ICCFD13-2026-271

Performance Assessment of Poisson-Free Incompressible Flow Solvers on GPU Architectures

T. Yasuda*, I. Tanno**, T. Hashimoto***, Y. Tanaka****, K. Morinishi***** and N. Satofuka******
Corresponding author: tkyasuda@mech.usp.ac.jp
* The University of Shiga Prefecture, Japan.
** Tsukuba University of Technology, Japan.
*** Kindai University, Japan.
**** Toyo Tire Corporation, Japan.
***** Professor Emeritus of Kyoto Institute of Technology, Japan.
****** Professor Emeritus of Kyoto Institute of Technology and The University of Shiga Prefecture, Japan.

Abstract: In this study, Poisson-free incompressible flow solvers—including the Artificial Compressibility Method (ACM), the Kinetically Reduced Local Navier–Stokes (KRLNS) equation, the Entropically Damped Artificial Compressibility (EDAC) method, the Bulk-Viscosity-Tuned Artificial Compressibility Method (BVACM) , and the Lattice Boltzmann Method (LBM)—are applied to three-dimensional homogeneous isotropic turbulence on the same GPU platform to compare their computational efficiency. All simulations are conducted at a fixed Reynolds number of Re = 4000. For $256 \times 256 \times 256$ grid, fourth-order ACM, KRLNS, EDAC and BVACM achieves higher computational speed than both the fractional step method (FSM) and LBM at the same L_2-norm error. Its high-order spatial discretization reduces phase errors, and RK4 time integration allows larger steps. For $128 \times 128 \times 128$ grid, BVACM is more efficient than LBM by damping high-frequency components via bulk viscosity, preserving large-scale structures while improving stability.

Keywords: Poisson-Free Solver, Artificial Compressibility Method, Lattice Boltzmann method, GPU Computation, Homogeneous Isotropic Turbulence, Bulk Viscosity–tuned ACM.

1. Introduction

With recent advances in computer technology, computational fluid dynamics (CFD) has achieved remarkable progress. To date, CFD has been widely applied to the analysis of incompressible and compressible flows, laminar and turbulent flows, multiphase flows, aeroacoustics, viscoelastic fluids, and magnetohydrodynamics, as well as to fluid–structure interaction, chemically reacting flows, multiphase and thermal flows, and environmental fluid dynamics. Through these applications, CFD has made significant contributions to the reproduction of complex flow phenomena and the elucidation of their underlying mechanisms.

In recent years, further acceleration through artificial intelligence (AI) and graphics processing units (GPUs), as well as applications to digital twins and optimal design, has been actively pursued. Consequently, the scope of CFD applications has expanded beyond engineering to include medical, environmental, and energy-related fields. At the same time, societal demands such as the reduction of environmental impact, the realization of a sustainable society, and the advancement of medical devices have been increasing. In response, improving the accuracy and efficiency of devices, effective energy utilization, and noise reduction have become critical technical challenges. To address these issues, the importance of CFD, which enables the understanding and optimization of fluid phenomena, is expected to further increase in the future.

Focusing on the evolution of computing systems, architectures have progressed from early scalar processors to vector processors, and currently to massively parallel computing using a large number of CPUs and GPUs. Accordingly, the development of algorithms suitable for parallel computation that can fully exploit modern computer architectures has become a key issue in improving the computational efficiency of CFD. In unsteady incompressible flow analysis, the continuity equation in the governing Navier–Stokes (NS) equations does not contain a time-derivative term. Therefore, methods in which the divergence-free condition is satisfied by solving a pressure Poisson equation have been widely used rather than directly solving the continuity equation. However, implicit solvers for the Poisson equation require global data communication across the computational domain, which leads to communication costs dominating the total computational cost in large-scale parallel computations. To overcome this drawback, artificial compressibility methods (ACM) [1], equations,and the lattice Boltzmann method (LBM) [2] have attracted increasing attention in recent years. Both methods eliminate the need to solve the pressure Poisson equation and allow pressure or velocity fields to be determined locally, making them well suited for parallel computation.

In the ACM approach, an artificial compressibility term is introduced into the continuity equation, and the pressure field is obtained through a time-marching procedure. In the incompressible limit, the speed of sound tends to infinity; by introducing a pseudo sound speed, the stiffness of the governing equations can be alleviated, enabling stable convergence to steady-state solutions. Subsequently, the dual time-stepping method was developed, in which pseudo-time iterations are performed within each physical time step, thereby extending the applicability of the artificial compressibility method to unsteady flows.

Following the development of the original artificial compressibility method, the Kinetically Reduced Local Navier–Stokes (KRLNS) method [3, 4] was proposed based on thermodynamic theory and demonstrated favorable numerical stability and computational efficiency. Subsequently, pressure-evolution approaches such as the Entropically Damped Artificial Compressibility (EDAC) method [5], generalized pressure-evolution formulations (often referred to as generalized pressure equation (GPE) frameworks)[6], and bulk-viscosity-based formulations such as the Bulk-Viscosity-Tuned Artificial Compressibility Method (BVACM) [7] have been developed to suppress artificial pressure waves and improve numerical stability. Owing to these developments, local pressure-evolution approaches that avoid the global solution of a pressure Poisson equation have attracted renewed attention as efficient and highly parallelizable methods for incompressible flow simulations.

In parallel, the Lattice Boltzmann Method (LBM), which also originates from kinetic theory, has emerged as an alternative framework for fluid-flow simulations. In LBM, the macroscopic flow field is obtained through the evolution of particle velocity distribution functions governed by advection and collision processes on a discrete velocity lattice. Through Chapman–Enskog analysis, LBM recovers the incompressible Navier–Stokes equations in the low-Mach-number limit. Owing to its kinetic-theory foundation, LBM offers several advantages, including low numerical dissipation in advection and high flexibility for complex flows such as multiphase, multicomponent, and non-Newtonian fluid systems. Furthermore, developments such as the Multiple Relaxation Time (MRT) model [8], Entropic LBM (ELBM) [9], Cascaded LBM [10], and Cumulant LBM [11] have significantly improved stability and accuracy, even at high Reynolds numbers.

Although the effectiveness of these methods has been widely reported [12, 13, 14, 15, 16, 17], studies that directly compare these methods under identical conditions remain limited. In particular, there are few studies that quantitatively compare computational accuracy and efficiency on GPU architectures and identify the optimal method for incompressible flow analysis. In this study, Poisson-free approaches, including ACM and its variants (EDAC and BVACM), the KRLNS equations, and the LBM, as well as the fractional-step method (FSM) that solves the pressure Poisson equation, are applied to three-dimensional homogeneous isotropic turbulence. By comparing all methods under identical computational conditions and on the same hardware platform, this study aims to provide guidelines for selecting an appropriate parallel computing method for incompressible flow analysis. Qualitative validation of the simulations is performed through visual comparisons of cross-sectional enstrophy fields, while quantitative evaluation is

carried out using global enstrophy, energy spectra and total kinetic energy. Furthermore, computational efficiency is assessed by comparing the computational time required for each method to achieve a comparable L_2-norm error level of the velocity field.

2. Numerical Methods and Computational Setup

2.1 Artificial Compressibility Method(ACM)

The ACM introduces an artificial compressibility term into the continuity equation of the incompressible Navier–Stokes equations, enabling pressure to be obtained through time evolution as follows:

$$\frac{\partial p}{\partial t} = -\beta \frac{\partial u_i}{\partial x} \tag{1}$$

$$\frac{\partial u_i}{\partial t} + \frac{\partial u_i u_j}{\partial x_j} = -\frac{\partial p}{\partial x_i} + \frac{1}{Re}\frac{\partial^2 u_i}{\partial x_j^2} \tag{2}$$

Here, $\beta(= 1/\mathrm{Ma}^2)$ denotes the artificial speed of sound (pseudo speed of sound). In the limit as β approaches infinity, the incompressibility condition, $\nabla \cdot u = 0$, is recovered. In this approach, the pressure field is relaxed along a pseudo-time direction, which allows incompressible flows with constant density to be treated explicitly. In this study, the commonly used dual time-stepping method for ACM is not adopted. Instead, stable computations are achieved by assuming a low Mach number and selecting a sufficiently small physical time step. This approach makes it possible to approximately and accurately simulate unsteady incompressible flows without iterative procedures in the pseudo-time direction. In addition, ACM allows for explicit treatment of pressure–velocity coupling, which simplifies implementation and provides excellent parallel efficiency in large-scale computations. On the other hand, the choice of the artificial speed of sound β and the time step size significantly affects the numerical stability and convergence. Therefore, selecting the appropriate parameters is a critical aspect of this method.

2.2 The Kinetically Reduced Local Navier-Stokes equations (KRLNS)

The form of KRLNS equations was proposed as an alternative thermodynamic description of incompressible fluid flows. Instead of directly solving the continuity equations, the KRLNS approach employs local evolution equations for the grand potential G:

$$\frac{\partial G}{\partial t} = -\beta \frac{\partial u_i}{\partial x_i} + \frac{1}{Re}\frac{\partial^2 G}{\partial x_j^2} \tag{3}$$

$$G = p - \frac{1}{2}\rho u_i^2 \tag{4}$$

By replacing the pressure with the grand potential, the method ensures that the incompressibility condition is naturally recovered during the time evolution, eliminating the need for a global Poisson equation. As a result, KRLNS achieves fully local computations with excellent parallel scalability while maintaining accuracy comparable to the incompressible Navier–Stokes equations for low-Mach-number flows. Owing to these advantages, the KRLNS framework has attracted attention as a promising and computationally efficient approach for incompressible flow simulation.

2.3 The Entropically Damped Artificial Compressibility method (EDAC)

In ACM, the introduction of artificial compressibility into the continuity equation inevitably generates pseudo-acoustic waves, which appear as high-frequency pressure oscillations in numerical solutions. These spurious pressure modes can deteriorate solution quality, particularly in low-Mach-number flows where accurate pressure prediction is essential. To address this issue, The EDAC method was proposed as an alternative to the conventional ACM. Instead of assuming isentropic behavior, EDAC allows entropy

generation and reduces density fluctuations, leading to a pressure-diffusion term that suppresses pseudo-acoustic waves while preserving the advantages of the artificial-compressibility framework. As a result, EDAC provides a more stable and robust formulation for incompressible-flow simulations, especially in situations where pressure fluctuations must be minimized. The governing equation for the pressure field in EDAC is given by

$$\frac{Dp}{Dt} = -\beta \frac{\partial u_i}{\partial x_i} + \frac{1}{Re} \frac{\partial^2 p}{\partial x_j^2} \tag{5}$$

In this formulation, the second term on the right-hand side represents a diffusion-based damping mechanism that dissipates high-frequency pressure oscillations. This entropy-stable damping effectively suppresses pseudo-acoustic waves and enhances numerical stability while retaining the advantages of the artificial-compressibility approach. In the present study, the convective term of the pressure in the equation (5) is neglected for the low-Mach-number assumption. As a result, the governing equation reduces to a form that is essentially equivalent to the GPE [6].

2.4 The Bulk-Viscosity Tuned Artificial Compressibility Method (BVACM)

As an alternative approach for damping compressible waves, the BVACM introduces a bulk-viscosity term into the momentum equation. This additional term is designed to artificially enhance the dissipation of dilatational motions, which are responsible for the propagation of compressible pressure waves in weakly compressible flow solvers. The modified momentum equation is expressed as

$$\frac{\partial u_i}{\partial t} + \frac{\partial u_i u_j}{\partial x_j} = -\frac{\partial p}{\partial x_i} + \frac{1}{Re} \frac{\partial^2 u_i}{\partial x_j^2} + \frac{A}{Re} \frac{\partial}{\partial x_i} \left(\frac{\partial u_j}{\partial x_j} \right) \tag{6}$$

$$A = \frac{\mu}{\zeta} + \frac{1}{3} \tag{7}$$

where,μ and ζ is the shear and bulk viscosity of the fluid, respectively. The bulk-viscosity parameter A is tuned to enhance numerical stability. Since the bulk viscosity term contains the divergence of the velocity, it becomes zero when the incompressibility condition is strictly satisfied. However, in practical ACM simulation, a small degree of compressibility is allowed. Consequently, the bulk-viscosity term remains non-zero and acts to suppress compressible waves and accelerate convergence. This residual contribution plays an important role: it selectively damps dilatational components of the flow, suppresses non-physical pressure fluctuations, and accelerates the convergence toward a quasi-incompressible state. In this sense, the bulk-viscosity mechanism acts as a numerical stabilization strategy that improves robustness without significantly altering the solenoidal part of the velocity field.

2.5 The Lattice Boltzmann Method (LBM)

The LBM is a numerical approach that describes fluid behavior through the processes of streaming and collision of velocity distribution functions defined along discrete velocity directions on a lattice. This method is a mesoscopic approach in which macroscopic fluid variables are derived from the moments of the distribution functions. Through the Chapman–Enskog expansion, it has been shown that, in the low-Mach-number regime, LBM approximately satisfies the incompressible Navier–Stokes equations. The fundamental Lattice Boltzmann Equation (LBE), assuming a BGK (Bhatnagar–Gross–Krook) collision operator, is written as follows:

$$f_i \left(\mathbf{x} + \mathbf{e}_i \Delta, t + \Delta t \right) = f_i \left(\mathbf{x}, t \right) - \frac{1}{\tau} \left(f_i \left(\mathbf{x}, t \right) - f_i^{eq} \left(\mathbf{x}, t \right) \right) \tag{8}$$

$$\rho = \sum_i f_i \tag{9}$$

Here, f_i denotes the velocity distribution function corresponding to the discrete velocity direction τ is the relaxation time, and f_i^{eq} is the local equilibrium distribution function. The left-hand side of the equation represents the streaming process, while the relaxation term on the right-hand side represents the collision process driving the system toward local equilibrium. Macroscopic physical quantities such as density and velocity are obtained from the moments of the distribution functions as follows:

$$\rho \mathbf{u} = \sum_i f_i \mathbf{e}_i \tag{10}$$

LBM possesses an algorithmic structure based on local lattice operations, which makes it highly suitable for parallel computation. In addition, due to its ease of boundary-condition implementation and adaptability to complex geometries, LBM has been widely used in numerical simulations of incompressible flows.

2.6 Test Problem and Computational Setup

In this study, numerical simulations were performed for three-dimensional homogeneous isotropic decaying turbulence. As the initial condition, turbulent flow field data constructed by Kida et al.[18] were employed. A regular Cartesian grid was used for the computational domain, with a grid resolution of $256 \times 256 \times 256$. Periodic boundary conditions were imposed in all directions. The Reynolds number was set to 4000. For FSM, ACM, KRLNS, EDAC, and BVACM, fourth-order Runge–Kutta (RK4) time integration [19] is employed for both second- and fourth-order spatial discretizations, while second- and fourth-order central difference schemes were used for spatial discretization. The Mach number was primarily fixed at 0.04. To examine the influence of the Mach number, three values, Ma = 0.01, 0.04, and 0.1, were employed. In the LBM simulation, D3Q27 model was used as velocity model. The simulations were executed on GPUs, and OpenACC was used to parallelize and accelerate the code. The GPU computations were performed on NVIDIA A30 GPU.

3. Results and Discussions

3.1 Simulation using $256 \times 256 \times 256$ grid

3.1.1 Comparison of Flow Fields and Statistical Quantities

To verify the numerical accuracy of each method, Figure 1 and Figure 2 show the time evolution of enstrophy and the energy spectra of total energy for second- and fourth-order special discretizations, respectively. Results obtained by the pseud-spectral method (PSM) and the fractional step method (FSM) are included for reference. When the enstrophy computed using FSM, ACM, KRLNS, EDAC, and BVACM with second-order spatial accuracy are compared with that obtained using PSM, the amplitudes remain similar, whereas the waveform shapes differ significantly for Time ($t^* = 2\pi Ut/L$) > 0.3. The energy spectra also deviate from PSM, particularly in the intermediate wavenumber range. These results suggest that, under the present conditions, the observed discrepancies are mainly caused by dispersive (phase) errors rather than dissipative errors. When fourth-order central differencing is used for the spatial discretization, the phase errors are significantly reduced, which supports this interpretation. In contrast, LBM shows good agreement with PSM regarding the phase of their temporal evolution; however, the maximum enstrophy is systematically smaller, and attenuation is observed on the high-wavenumbers in the energy spectrum. This behavior is likely attributed to the single-relaxation-time BGK model in LBM, which induces excessive dissipation (hyperviscosity) at high wavenumbers. Figure 3 shows the enstrophy fields on the x–y plane at z=1/4L and t^*= 0.5. A similar tendency is observed in the enstrophy distribution: the enstrophy patterns obtained by FSM, ACM, KRLNS, EDAC, and BVACM with second order spatial accuracy differ from that of PSM, whereas those with fourth order accuracy agree well with PSM. The enstrophy pattern obtained by LBM is similar to that of PSM, but the enstrophy magnitude is weaker.

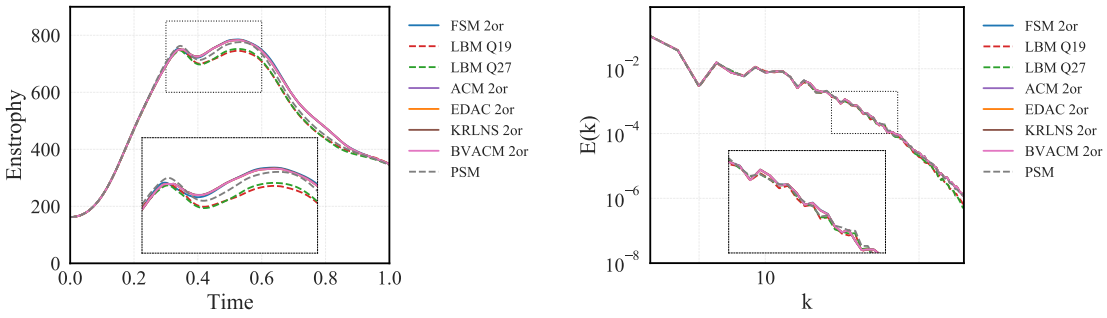

Figure 1: Time evolution of a enstrophy and a total energy spectra at t^*=0.5 (2nd order discretization)

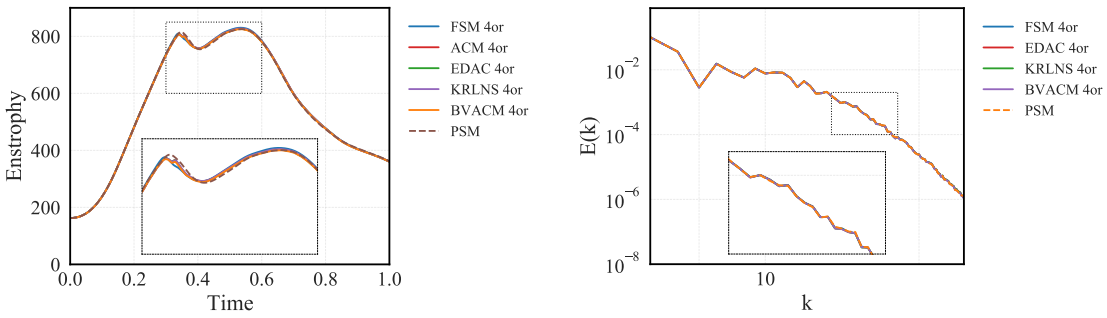

Figure 2: Time evolution of a enstrophy and a total energy spectra at t^*=0.5 (4th order discretization)

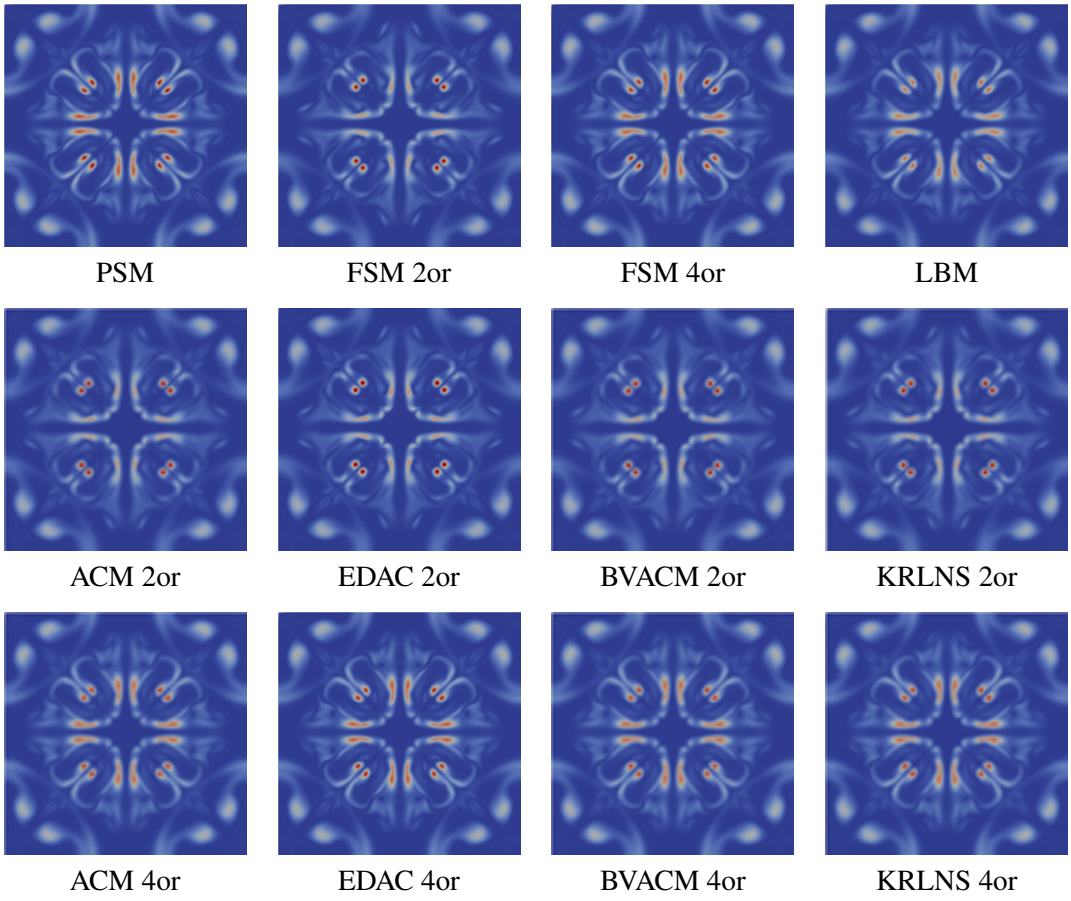

Figure 3: Comparison of enstrophy field obtained by different numerical methods.

Figure 4 shows the time evolution of the total energy. Although the differences in total energy among the methods are generally small, oscillations are observed in the initial stage of the simulation for all methods except FSM. These oscillations occur for both second- and fourth-order spatial accuracy and are therefore independent of the formal order of accuracy. As all methods except FSM introduce artificial compressibility, the oscillations are considered to result from acoustic waves excited at the beginning of the simulation, which subsequently affect the total energy. Furthermore, no significant difference is observed between ACM, KRLNS, EDAC in terms of the decay of these acoustically induced oscillations. This suggests that the pressure oscillations observed under the present conditions are not local high-frequency noise but rather global oscillations extending over the entire computational domain.

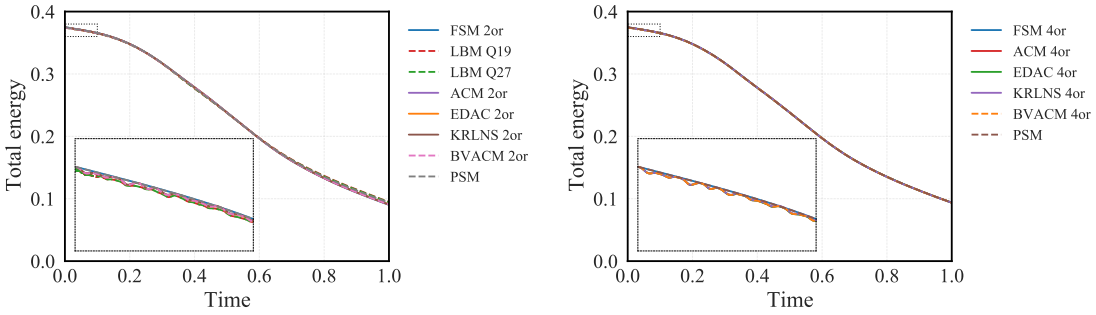

Figure 4: Time evolution of a total energy

3.1.2 Effect of Mach number

To examine the influence of the Mach number, the time evolution of enstrophy, and the energy spectrum, the total energy is presented for the EDAC simulations with Ma = 0.01, 0.04, and 0.1 in Figure 5. From the figures, it is observed that variations in the Mach number have little influence on the enstrophy or the energy spectrum, whereas the amplitude of the initial oscillations in total energy increases as the Mach number becomes larger. This behavior is attributed to the fact that, with increasing Mach number, the contribution of artificial compressibility to the flow field becomes more significant, leading to stronger acoustic waves excited at the early stage of the computation.

3.2 Simulation using $128 \times 128 \times 128$ grid

Simulations in the case using a $128 \times 128 \times 128$ computational grid were also performed. Both BVACM and LBM were able to converge to a solution under these conditions. Figure 6 presents the time evolution of enstrophy and the energy spectra obtained using BVACM with different bulk-viscosity values and using LBM. The results demonstrate that reducing the bulk viscosity in BVACM brings the results closer to those of PSM. Whereas LBM exhibits more pronounced damping, resulting in lower enstrophy. Figure 7 shows the enstrophy colormaps for different bulk-viscosity values in BVACM. The resulting enstrophy pattern is similar to that obtained using second-order spatial accuracy on a 256-grid computation, and large bulk viscosity leads to excessive numerical dissipation and weakens the enstrophy pattern.

3.3 Computational efficiency

Next, the computational efficiency of each method is compared based on computational time and numerical error, as summarized in Table 1 . In calculations using a $256 \times 256 \times 256$ grid, ACM, KRLNS, EDAC and BVACM with fourth-order spatial accuracy exhibit higher computational speed than FSM and LBM for comparable L_2-norm error. This may be partly because FSM requires the solution of a global Poisson equation, which limits scalability in parallel computations. In contrast, the 27-velocity LBM increases computational cost due to factors such as the need to update 27 distribution functions per lattice node and the non-coalesced memory access patterns arising from the directional streaming process. Its

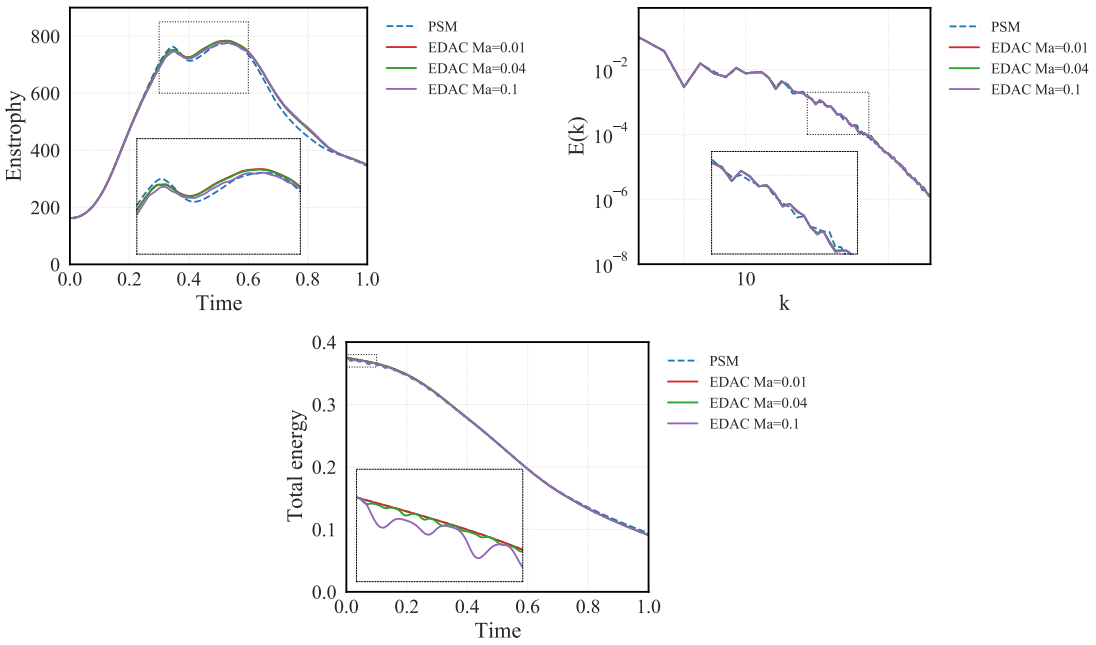

Figure 5: Effect of Ma on a enstrophy, a total energy spectra and a total energy

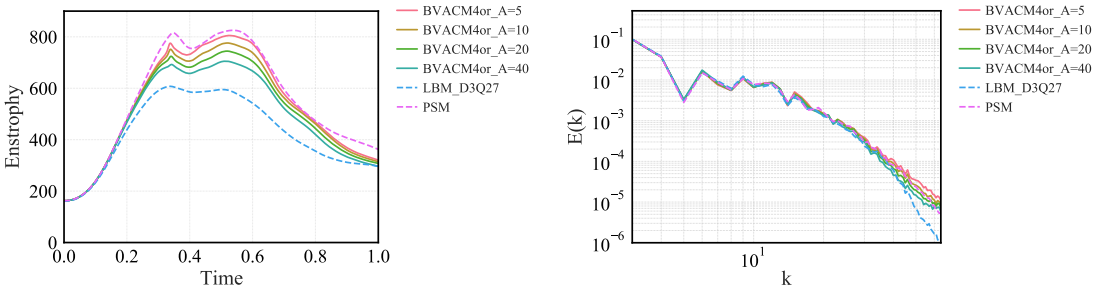

Figure 6: Time evolution of a enstrophy and a total energy spectra at t^*=0.5 (128^3 grid)

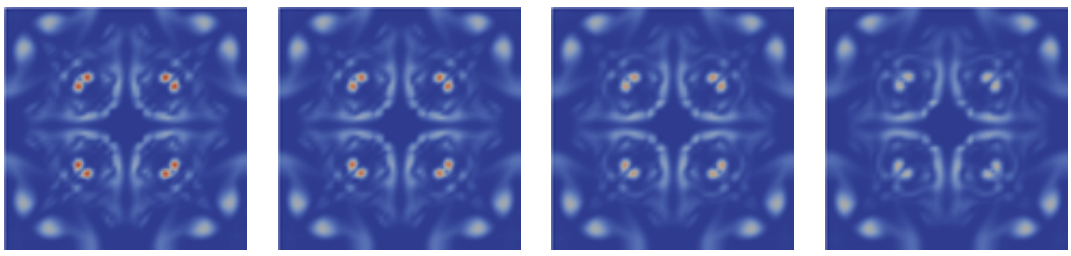

Figure 7: Comparison of enstrophy field obtained by BVACM at $z/L = 0.25$ (4th-order, 128^3 grid)

Table 1: CPU time and L_2-norm error for velocity

Solver	Order of accuracy	Number of grid	CPU time [sec]	Number of time steps	CPU time per time step [sec]	L_2-norm error (Velocity)
FSM	4th	256^3	553	500	1.107	0.033
ACM	2nd	256^3	48	5000	0.010	0.180
ACM	4th	256^3	72	6000	0.012	0.039
EDAC	4th	256^3	72	6000	0.012	0.039
KRLNS	4th	256^3	80	6000	0.013	0.040
BVACM	4th	256^3	125	6000	0.021	0.039
BVACM	4th	128^3	8	3000	0.003	0.218
LBM (D3Q27)	2nd	256^3	189	11085	0.049	0.046
LBM (D3Q27)	2nd	128^3	15	5543	0.003	0.192

time step is also fixed by the prescribed Mach number, requiring more steps to reach the same physical time, whereas ACM, KRLNS, EDAC and BVACM use fourth-order Runge–Kutta integration, allowing larger steps and fewer updates. In simulations using $128 \times 128 \times 128$ grid, BVACM is faster than LBM, damping high-frequency components to preserve large-scale structures and maintain an L_2-norm error comparable to a second-order method on a $256 \times 256 \times 256$ grid.

4. Conclusions

In this study, ACM, EDAC, BVACM, KRLNS, LBM and FSM were compared under identical conditions for three-dimensional homogeneous isotropic turbulence, and their performance was evaluated in terms of both accuracy and computational efficiency. The results show that, for second-order spatial accuracy, ACM, KRLNS, EDAC, BVACM and FSM are affected by dispersive errors, whereas LBM exhibits relatively larger dissipative errors. It was also demonstrated that LBM yields smaller errors than the second-order spatial schemes. On the other hand, by adopting fourth-order spatial accuracy for ACM, KRLNS, EDAC, BVACM and FSM, dispersive errors are significantly reduced, and accuracy comparable to that of LBM is achieved. Fourth-order central-difference implementations of ACM using RK4 time integration on GPUs, were found to be the most computationally efficient for simulations using $256 \times 256 \times 256$ grid and BVACM for simulations using $128 \times 128 \times 128$ grid at comparable error levels. In homogeneous isotropic turbulence, the pressure-damping terms in EDAC and KRLNS had little effect due to the weak local pressure oscillations, but they may be more effective in wall-bounded or obstacle-laden flows where larger pressure fluctuations occur. Relative accuracy and dissipation may also change under such conditions. Moreover, the performance of higher-order LBM collision models, such as MRT, moment-based, and cumulant methods, remains to be evaluated, and future work should include these methods in comparative studies under wall-bounded or obstacle-laden flows.

References

[1] A. Chorin. A numerical method for solving incompressible viscous flow problems. *Journal of Computational Physics*, 2:12–26, 1976.

[2] P. L. Bhatnagar, E. P. Gross, and M. Krook. A model for collisional processes in gases i: Small amplitude processes in charged and neutral one-component systems. *Physical Review*, 94:511–525, 1954.

[3] I. V. Karlin, A. G. Tomboulides, C. E. Frouzakis, and S. Ansumali. Kinetically reduced local Navier–Stokes equations: An alternative approach to hydrodynamics. *Physical Review E*, 74:035702, 2006.

[4] S. Borok, S. Ansumali, and I. V. Karlin. Kinetically reduced local Navier–Stokes equations for simulation of incompressible viscous flows. *Physical Review E*, 76:066704, 2007.

[5] J. R. Clausen. Entropically damped form of artificial compressibility for explicit simulation of incompressible flow. *Physical Review E*, 87:013309, 2013.

[6] A. Toutant. General and exact pressure evolution equation. *Physics Letters A*, 381(44):3739–3742, 2017.

[7] T. Yasuda, I. Tanno, T. Hashimoto, K. Morinishi, and N. Satofuka. Artificial compressibility method using bulk viscosity term for an unsteady incompressible flow simulation. *Computers and Fluids*, 258:105885, 2023.

[8] D. d'Humières. Generalized lattice Boltzmann equations. *Rarefied Gas Dynamics: Theory and Simulations*, 159:450–458, 1992.

[9] I. V. Karlin, A. N. Gorban, S. Succi, and V. Boffi. Maximum entropy principle for lattice kinetic equations. *Physical Review Letters*, 81(1):6–9, 1998.

[10] M. Geier, A. Greiner, and J. G. Korvink. Cascaded digital lattice Boltzmann automata for high reynolds number flow. *Physical Review E*, 73:066705, 2006.

[11] M. Geier, M. Schönherr, A. Pasquali, and M. Krafczyk. The cumulant lattice Boltzmann equation in three dimensions: Theory and validation. *Computers and Mathematics with Applications*, 70:507–547, 2015.

[12] T. Ohwada and P. Asinari. Artificial compressibility method revisited: Asymptotic numerical method for incompressible Navier–Stokes equations. *Journal of Computational Physics*, 229:1698–1723, 2010.

[13] T. Ohwada, P. Asinari, and D. Yabusaki. Artificial compressibility method and lattice Boltzmann method: Similarities and differences. *Computers and Mathematics with Applications*, 61:3461–3474, 2011.

[14] T. Yasuda, T. Hashimoto, I. Tanno, Y. Tanaka, H. Minagawa, K. Morinishi, and N. Satofuka. Effect of collision and velocity model of lattice Boltzmann model on three-dimensional turbulent flow simulation. *International Journal of Computational Fluid Dynamics*, 31(4–5):258–268, 2017.

[15] A. Toutant. Numerical simulations of unsteady viscous incompressible flows using general pressure equation. *Journal of Computational Physics*, 374:822–842, 2018.

[16] T. Hashimoto, T. Yasuda, I. Tanno, Y. Tanaka, K. Morinishi, and N. Satofuka. Multi-GPU parallel computation of unsteady incompressible flows using kinetically reduced local Navier–Stokes equations. *Computers and Fluids*, 167:215–220, 2018.

[17] X. Shi and C. A. Lin. Simulations of wall-bounded turbulent flows using general pressure equation. *Flow, Turbulence and Combustion*, 105:67–82, 2020.

[18] S. Kida and Murakami Y. Kolmogorov similarity in freely decaying turbulence. *Physics of Fulids*, 30:2030–2039, 1987.

[19] A. Jameson and T. J. Baker. Solution of the euler equations for complex configurations. In *AIAA Paper*, number 83-1929, 1983.